Research in Astronomy and Astrophysics, 24:035012 (15pp), 2024 March https://doi.org/10.1088/1674-4527/ad057b

Confirmation of a Sub-Saturn-size Transiting Exoplanet Orbiting a G Dwarf: TOI-1194 b and a Very Low Mass Companion Star: TOI-1251 B from TESS

Jia-Qi Wang[1,2], Xiao-Jun Jiang[1,2], Jie Zheng[1], Hanna Kellermann[3,4], Arno Riffeser[3], Liang Wang[2,5,6], Karen A. Collins[7], Allyson Bieryla[7], Lars A. Buchhave[8], Steve B. Howell[9], Elise Furlan[10], Eric Girardin[11], Joao Gregorio[12], Eric Jensen[13], Felipe Murgas[14,15], Mesut Yilmaz[16], Sam Quinn[7], Xing Gao[17,18], Ruo-Yu Zhou[19], Frank Grupp[3,4], and Hui-Juan Wang[1,2]
[1] CAS Key Laboratory of Optical Astronomy, National Astronomical Observatories, Chinese Academy Of Sciences, Beijing 100101, China; wanghj@nao.cas.cn
[2] University of Chinese Academy of Sciences, Beijing 100049, China
[3] University Observatory Munich, Scheinerstrasse 1, D-81679 Munich, Germany; frank.grupp@lmu.de
[4] Max Planck Institute for Extraterrestrial Physics, Giessenbachstr. 1, D-85748 Garching, Germany
[5] National Astronomical Observatories/Nanjing Institute of Astronomical Optics & Technology, Chinese Academy of Sciences, Nanjing 210042, China
[6] CAS Key Laboratory of Astronomical Optics & Technology, Nanjing Institute of Astronomical Optics & Technology, Nanjing 210042, China
[7] Center for Astrophysics, Harvard & Smithsonian, 60 Garden Street, Cambridge, MA 02138, USA
[8] National Space Institute, Technical University of Denmark, Elektrovej, DK-2800 Kgs. Lyngby, Denmark
[9] NASA Ames Research Center, Moffett Field, CA 94035, USA
[10] NASA Exoplanet Science Institute, Caltech/IPAC, Mail Code 100-22, 1200 E. California Blvd., Pasadena, CA 91125, USA
[11] Grand Pra Observatory, Switzerland
[12] Department of Physics, Washington University, St. Louis, MO 63130, USA
[13] Department of Physics and Astronomy, Swarthmore College, Swarthmore, PA 19081, USA
[14] Instituto de Astrofísica de Canarias (IAC), E-38205 La Laguna, Tenerife, Spain
[15] Departamento de Astrofísica, Universidad de La Laguna, Tenerife, Spain
[16] Dept. of Astronomy and Space Sciences, Ankara University, Tandogan 06100 Ankara, Turkey
[17] Xinjiang Astronomical Observatory, Chinese Academy of Sciences, Urumqi 830011, China
[18] Urumqi No.1 Senior High School, Urumqi 830002, China
[19] Lijiang Gemini Observatory, Lijiang 674199, China
Received 2023 July 12; revised 2023 September 28; accepted 2023 October 18; published 2024 February 26

Abstract

We report the confirmation of a sub-Saturn-size exoplanet, TOI-1194 b, with a mass of about $0.456^{+0.055}_{-0.051}\,M_{\rm J}$, and a very low mass companion star with a mass of about $96.5 \pm 1.5\,M_{\rm J}$, TOI-1251 B. Exoplanet candidates provided by the Transiting Exoplanet Survey Satellite (TESS) are suitable for further follow-up observations by ground-based telescopes with small and medium apertures. The analysis is performed based on data from several telescopes worldwide, including telescopes in the Sino-German multiband photometric campaign, which aimed at confirming TESS Objects of Interest (TOIs) using ground-based small-aperture and medium-aperture telescopes, especially for long-period targets. TOI-1194 b is confirmed based on the consistent periodic transit depths from the multiband photometric data. We measure an orbital period of 2.310644 ± 0.000001 days, the radius is $0.767^{+0.045}_{-0.041}\,R_{\rm J}$ and the amplitude of the RV curve is $69.4^{+7.9}_{-7.3}\,{\rm m\,s^{-1}}$. TOI-1251 B is confirmed based on the multiband photometric and high-resolution spectroscopic data, whose orbital period is $5.963054^{+0.000002}_{-0.000001}$ days, radius is $0.947^{+0.035}_{-0.033}\,R_{\rm J}$ and amplitude of the RV curve is $9849^{+42}_{-40}\,{\rm m\,s^{-1}}$.

Key words: planets and satellites: fundamental parameters – planets and satellites: gaseous planets – stars: fundamental parameters – stars: low-mass – methods: data analysis – techniques: photometric – techniques: spectroscopic

1. Introduction

Since the discovery of PSR 1257+12 c and d in 1992 (Rasio et al. 1992), more than 5000 planets have been confirmed. Ground-based and space-based telescopes have significantly contributed to exoplanet detection and research. The expected efficiency of the transit method for exoplanet search is very optimistic (Horne 2003), but the actual situation in recent years shows that the rate of planet identification and the physical characteristics of the discovered planets are obviously limited by the detection methods and observation strategies. For instance, about 17% of confirmed planets revolve around their host star with an orbital period greater than 100 days,[20] which makes it more challenging to detect long-period and wide-orbit planets. These planets share similarities with our own solar system and require further research. Understanding these exoplanets and their properties can yield valuable insights into

[20] According to NASA Exoplanet Archive (Akeson et al. 2013), https://exoplanetarchive.ipac.caltech.edu/docs/counts_detail.html.

planetary formation and evolution. Therefore, the immediate goal is to expand the sample of detected planets through advanced detection methods and observation strategies.

The most efficient way to confirm exoplanets is through space-based surveys and follow-up studies from ground-based telescopes. The nine-year survey by the Kepler mission (Borucki et al. 2010; Howell et al. 2014) gives us a glimpse into the abundance of planets in the universe. Since the launch of Transiting Exoplanet Survey Satellite (TESS) in 2018 April, numerous exoplanet candidates have been discovered and confirmed. However, some candidates with extended periods ($\geqslant$27 days), or only a single transit detected (called single-transit, Cooke et al. 2018) require further confirmation and research, which may demand a considerable amount of observation time at a single ground-based site. In addition, capturing the full transit can be challenging in certain cases. A well-designed multi-telescope campaign provides a solution to this problem, and the feasibility of this approach has been validated by the studies on long-period planet HD 80606 b, which has a period of 111.43605 days (Naef et al. 2001; Pont et al. 2009). For instance, telescopes located at 40° latitude typically have an average dark time of around 8 hr per observation night. In this case, multiple telescopes spanning a time zone of fewer than eight hours can work together to perform relay observations on exoplanets with transit durations exceeding eight hours. By doing so, more data can be obtained with a single transit for these planets, which have larger orbital radii and a higher probability of being in the habitable zone.

Simultaneous multiband photometry using ground-based telescopes provides a cost-effective and efficient method for identifying exoplanet candidates and reducing false positives (FPs). While space-based telescopes capture the decline in candidate stars' luminosity through long-term sky area monitoring, the satellite orbit and observation conditions limit the available observation time to a single band, ensuring survey efficiency and the robustness of the telescope system. It is worth noting that over half of the exoplanet candidates are subject to stellar luminosity variations or are eclipsing binaries (EBs) (Deleuil & Fridlund 2018). Simultaneous multi-color light curves can effectively eliminate most FPs caused by EBs (Tingley 2004). In contrast, the Kepler mission has shown that low transit signal-to-noise ratios (S/Ns) are more likely to result in FPs, particularly in the case of Earth-like planets (Fressin et al. 2013). Although this issue also affects ground-based telescope detection, the ample observation time provides an opportunity to accumulate more time-series data on transits and enhance the transits' S/Ns by adding multiple transits (Kaltenegger & Traub 2009).

Since the first transit planet was confirmed (Charbonneau et al. 2000), photometry of transits has become the most efficient method for identifying new planet candidates and determining their radius (R_P) and semimajor axis (a). Achieving 1% precision in radius determination is essential for studies of planetary structure and evolution, and relies heavily on accurate measurements of stellar limb darkening values (Csizmadia et al. 2013). Transit light curve morphology, particularly the ingress and egress fragments, can significantly impact model-estimated parameters. The transit observation cadence is the primary driver for such morphology (Kipping 2010). Ground-based telescopes with meter-scale apertures (called one meter-class telescopes) enable high S/Ns $\geqslant$ 100 for follow-up observations, while maintaining an observation cadence that conforms to exposure time constraints.

We want to present some of our latest confirmations of TOI-1194 b and TOI-1251 B through our global follow-up campaign utilizing several telescopes, including the Sino-German multi-band photometric campaign. Section 2 offers an introduction to the Sino-German multiband photometric campaign, target selection and the follow-up observation strategy employed during our campaign. Section 3 gives an overview of the observations. Section 4 describes the rapid processing of intensive data generated by campaign telescopes and light curve fitting, while Section 5 details our confirmation of TOI-1194 b and TOI-1251 B. Lastly, Section 6 concludes with a summary and discussion of our findings.

2. Sino-German Multiband Photometric Campaign

In order to identify a greater number of long-period planets, our Sino-German cooperation team has successfully established a global multiband follow-up observation network. This network incorporates a wide range of optical observational equipment, including both professional-grade instruments and those utilized by amateur astronomers. The network remains distributed across several telescopes in China, Germany and Chile, covering time zones spanning five to twelve hours among the sites, as illustrated in Figure 1. Currently, the network includes fifteen telescopes located at ten observation sites.

Our follow-up campaign utilizes multiband photometric observations to exclude FPs from Tess Objects of Interest (TOIs) we have observed. Nonetheless, filter systems may differ among several telescopes. For instance, telescopes at Xinglong (Huang et al. 2012; Fan et al. 2016; Bai et al. 2018) and Weihai (Hu et al. 2014; Gao et al. 2016) in China use the Johnson-Cousins filter system, while telescopes at Wendelstein Observatory in Germany (Hopp et al. 2014; Steuer et al. 2021) and Nanshan in China utilize the SDSS $u'g'r'i'z'$ system. Other amateur telescopes rely on RGB filters or white band (refer to Table 1).

2.1. Target Selection and Observation Strategy

To confirm exoplanets, obtaining high-quality data depends upon choosing candidates with full-transit when observation conditions are favorable. More than half of the TOI objects have brightness above 12 mag in the TESS band, making them suitable for observation using one meter-aperture telescopes.

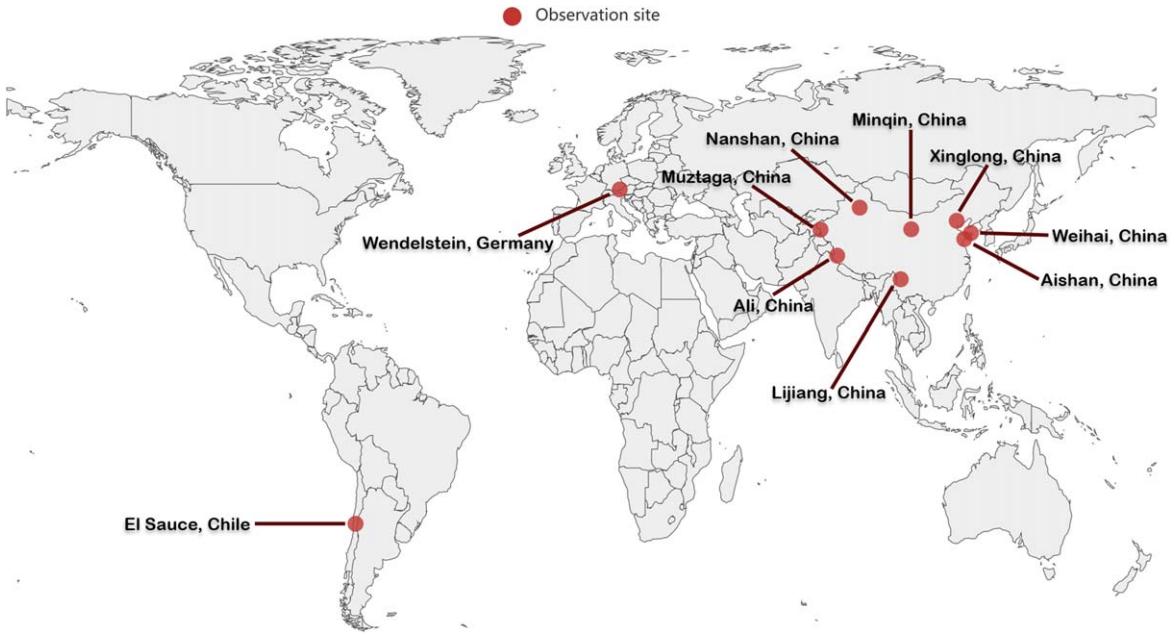

Figure 1. Location of each site in the campaign.

Table 1
Primary Parameters of Telescopes in Sino-German Campaign

Site	Longitude (°)	Latitude (°)	Altitude (m)	Aperture (cm)	Filter	FoV.
Nanshan, China	87.1736E	43.4747N	2088	25/60	SDSS $g'r'i'$	62′/25′
Aishan, China	119.9453E	36.1231N	100	10/25	LRGB	50′/87′
Weihai, China	122.0496E	37.5359N	100	60/100	Johnson *BVRI*	30′/12′
Lijiang, China	100.0300E	26.6951N	3200	30/35	SDSS $g'r'i'$/LRGB	21′/25′
El Sauce, Chile	70.7631W	30.4725S	1525	35/60	LRGB	60′/60′
Xinglong, China	117.5772E	40.3958N	950	60/80/85	Johnson *BVRI*	37′/11′/30′
Wendelstein, Germany	12.0121E	47.7364N	1838	43	SDSS $g'r'i'$	43′
Ali, China	80.1272E	32.2312N	5360	50	Johnson *BVRI*	11′
Muztaga, China	74.8967E	38.3297N	4583	50	Johnson *V*	5′
Minqin, China	103.3152E	38.4141N	1335	60	Johnson *BVRI*	30′

During the Sino-German campaign follow-up observations, our strategy aims to maximize the observation efficiency within the limited observation time. Our team achieves this efficient observation strategy by calculating all TOI transits for each observation site during the observable time. The TOIs are then ranked in terms of priorities based on observation parameters such as brightness, transit depth and orbital period. Between 2019 October and 2023 May, we screened and observed a total of 181 TOIs. Through our follow-up data, we confirmed a planet orbiting a solar-type star, TOI-1194 b, and a very low-mass stellar companion, TOI-1251 B.

For one meter-aperture telescopes, the main factor affecting the precision of photometric observation data is S/N. The point source standard S/N formula is as follows

$$\mathrm{S/N} = \frac{R_* \times t}{\sqrt{R_* \times t + n_{\mathrm{pix}} \times (R_{\mathrm{sky}} \times t + \mathrm{RN}^2 + D \times t)}}.$$

In this context, R_* denotes the target flux, t represents exposure time, R_{sky} indicates the sky background flux, n_{pix} signifies the number of pixels occupied by a star, RN refers to camera readout noise and D denotes dark current (Howell 2006). Due to the use of a camera cooler with temperature below −80 °C, dark current noise can be ignored. A faster readout speed results in greater readout noise, while a slower readout speed tends to be preferred. Analyses of CoRot and Kepler data by Kipping have revealed that sampling frequency has a

particularly crucial effect on planet confirmation and the determination of planetary parameters (Kipping 2010). Longer exposure cadences of photometry images can result in increasing levels of systematic errors concerning physical parameters. On the 60 cm telescope at Xinglong Observatory, we employed an Andor #DZ936N CCD camera with an S/N of 100 for a 12 mag star exposure lasting 10 s. By utilizing a readout speed of 1 MHz, the readout time per image was reduced to 4 s, albeit with a readout noise of 6.5 electrons. Conversely, the readout time was prolonged to 76.8 s and the readout noise reduced to 3.6 electrons at a readout speed of 50 kHz. Furthermore, we selected a gain value closest to 1 to curb readout noise linked to amplification. The CCD/CMOS exposure parameters were tailored to meet these standards and set for the telescope used during our campaign. Consequently, the photometric data obtained achieved an accuracy better than 0.002 mag when the S/N was no less than 100.

It is noteworthy that roughly 20% of the TOIs are brighter than eight in TESS band, making them well-suited for observation with one meter-class telescopes. However, when observing TOIs brighter than 8 mag, the field of view (FoV) of one-meter telescopes is typically limited to approximately 30′, making identification of reference stars with similar brightness within the FoV difficult. To ensure optimal data quality, it is imperative to appropriately defocus the target image in order to avoid saturation, while also limiting the exposure time to effectively enhance the S/N of fainter reference stars within the FoV. The efficacy of the observation strategy is critical to successful data acquisition.

3. Observations

We observed two planet candidates from TESS, TOI-1194.01 and TOI-1251.01, by using several ground-based one meter-class telescopes in the Sino-German campaign and TESS Follow-up Observing Program (TFOP).[21] The photometric observation parameters are summarized in Tables 3 and 4, followed by a description of the observations by different observatory sites and TESS.

3.1. TESS Observation

Sector 14 of the TESS observation marked the first discovery of TOI-1194 b and TOI-1251 B. TOI-1194 b was alerted as a candidate on 2019 August 27th, with 2 minute cadence data subjected to reduction by the Science Processing Operations Center (SPOC) pipeline (Jenkins et al. 2016). The resulting output showed evidence of a companion with a period of 2.31 days. We performed a check of the Simple Aperture Photometry (SAP) fluxes (Twicken et al. 2010; Morris et al. 2020) for TOI-1194 b in Sectors 14, 20, 21, 40, 41, 47, 48 and found no trace of additional companions.

TOI-1251 B was flagged as a candidate on 2019 October 17th, after reducing its 2 minute cadence data with the SPOC pipeline. Its high ecliptic latitude resulted in visibility across Sectors 14–26. The light curves indicated a companion with a period of 5.96 days. We searched for additional companions using the SAP fluxes in Sectors 14–26, 40–41, 48–49 and 51–52, but no others were detected.

[21] https://tess.mit.edu/followup/

Table 2
CCD Parameters of Telescopes at Xinglong Observatory Used in TOIs Follow-up Observations

Telescope	CCD Type	Readout Noise (e^- Rms)	Gain (e^- per A/D)	Pixel Scale ($''$ pixel^{-1})
60 cm	Andor DZ936N	6.5	1.1	1.10
80 cm	PYL1300BX	4.02	1.36	0.51
85 cm	Andor DZ936N	7.0	0.97	0.93

3.2. Ground-based Follow-up Photometric Observation

3.2.1. Xinglong Observatory

We obtained data from three telescopes at Xinglong Observatory, in Hebei, China, during the Sino-German follow-up campaign. Specifically, data from the 0.6 m telescope, TNT (0.8 m) (Huang et al. 2012) and NBT (0.85 m) (Bai et al. 2018) resulted in the acquisition of eight series of data (seven primary transits and one secondary transit) of TOI-1194 b and two series of data (all primary transits) for TOI-1251 B. We require that the S/Ns of the images are greater than 1000 pixel^{-1}, and the exposure times of each band are adjusted according to environmental conditions such as sky background and seeing, which are not fixed values.

The selected CCD exposure parameters are outlined in Table 2. Despite our efforts, the primary transit on 2021 December 2nd and secondary transit on 2022 March 1st of TOI-1194 b could not be satisfactorily captured due to poor photometric accuracy. Analysis of planetary parameters and properties was primarily based on the transit data outlined in Tables 3 and 4, which detail the observation date, filters and the number of images.

3.2.2. Canela's Robotic Observatory (CROW)

We conducted an observation of TOI-1194 b on 2019 December 28th in the SDSS g' band using the CROW 0.35 m telescope located in Portugal. The telescope is equipped with an ST-10XME camera and a pixel scale of 0.″66. The exposure time of each image is 180 s and the S/N value of the target star is greater than 850 pixel^{-1}. We obtained 58 data points

Table 3
Ground-based Photometric Follow-up Observation of TOI-1194 b

Date	Telescope	Band	Duration (minutes)	Number of Images
2019/10/16	PvdK 0.6 m	SDSS i'	200	58
2019/12/05	GdP 0.4 m	SDSS z'	295	107
2019/12/28	CROW 0.35 m	SDSS g'	249	58
2020/01/14	FLWO 1.2 m	*B*	244	424
2020/04/22	Xinglong 0.8 m	*BVRI*	246	314
2021/03/23	Xinglong 0.6 m	*BVRI*	149	182
2021/04/06	Xinglong 0.6 m	*BVRI*	128	190
2021/04/13	Xinglong 0.8 m	*BVRI*	144	424
2021/12/02[a]	Xinglong 0.8 m	*BVRI*	75	100
2022/02/21	Xinglong 0.85 m	*BVRI*	131	720
2022/02/28	Xinglong 0.6 m	*BVRI*	138	156
2022/03/01[b]	Xinglong 0.6 m	*BVRI*	165	476
				Total images: 3209

Notes.
[a] Ignored because of poor photometric quality.
[b] Secondary transit.

throughout the entire transit, which yielded photometric data analyzed using `AstroImageJ` (Collins et al. 2017) with rms = 0.001 mag precision.

3.2.3. Grand-Pra Observatory (GdP)

Our observation of TOI-1194 b on 2019 December 5th was conducted in the SDSS z' band using the RCO 0.4 m telescope located at the GdP in Switzerland. The telescope features an FLI4710 camera with a pixel scale of 0.″73. The exposure time is 150 s and S/N value of the target star is greater than 540 pixel^{-1}. We acquired 107 data points throughout the entire transit, enabling successful photometric analysis using `AstroImageJ` (Collins et al. 2017) with rms = 0.002 mag precision.

3.2.4. Fred Lawrence Whipple Observatory (FLWO)

On 2020 January 14th, we observed TOI-1194 b in the *B* band using the KeplerCam instrument mounted on the FLWO 1.2 m telescope, located at Mt. Hopkins in Arizona, USA. KeplerCam is a wide-field CCD camera constructed to provide multiband follow-up photometry for the Kepler Input Catalog (KIC), with a pixel scale of 0.″67; the four output amplifiers are read out in unison at 200 kHz; the total readout time and instrument overhead are 11 s when binned 2 × 2 (Szentgyorgyi et al. 2005). The exposure time is 15 s and S/N value of the target star is greater than 300 pixel^{-1}. We acquired 424 data points throughout the entire transit, which enabled us to conduct successful photometric analysis using `AstroImageJ` (Collins et al. 2017) with rms = 0.002 mag precision.

3.2.5. Peter Van De Kamp Observatory (PvdK)

We observed TOI-1194 b on 2019 October 5th, in the SDSS i' band by using the PvdK telescope, an f/7.8 Ritchey–Chrétien telescope located in Pennsylvania, USA, with an aperture of 0.6 m. The telescope employed an Apogee U16M camera, and the pixel scale is 0.″76 with 2 × 2 binning (Beatty et al. 2012). The exposure time was 98 s and S/N value of the target star was greater than 350 pixel^{-1}. The observation spanned the entire transit and yielded 58 data points, which were processed using `AstroImageJ` (Collins et al. 2017) with rms = 0.002 mag precision.

3.2.6. Ankara University Kreiken Observatory (AUKR)

We observed TOI-1251 B using the 0.8 m Prof. Dr. Berahitdin Albayrak Telescope (hereafter T80 Telescope) on 2019 October 12th and on 2020 August 17th from the AUKR Observatory in Turkey; both observations encompassed the entire transit. The T80 Telescope is equipped with an Apogee Alta U47 camera, and the pixel scale is 0.″8. The filter used on 2019 October 12th was *R* band, and the exposure time was 12 s so that the S/N value of the target star is greater than 200 pixel^{-1}. The observation on 2020 August 17th utilized SDSS g' and z' bands, and the exposure time in g' is 10 s so that the S/N value of the target star is greater than 100 pixel^{-1} and the exposure time in z' is 30 s so that the S/N value of the target star is greater than 250 pixel^{-1}. The images were analyzed using `AstroImageJ` (Collins et al. 2017) with rms = 0.004 mag precision in each band.

3.2.7. Teide Observatory (OT)

We observed TOI-1251 B on 2019 October 18th in the SDSS $g'r'i'z'$ bands using the MuSCAT2 camera mounted on the 1.52 m Telescopio Carlos Sánchez (TCS) telescope located at the OT in Tenerife, Spain. The primary mirror is fixed in an equatorial structure with a Cassegrain focus and focal length of f/13.8 in a Dall–Kirkham type configuration. MuSCAT2 has a capability of 4-color simultaneous imaging in SDSS $g'r'i'z'$, with a pixel scale of 0.″44 (Narita et al. 2019). The exposure time is 3 s in each band so that the S/N value is greater than 300 pixel^{-1}. Our observation covers full transit and yielded 765 points in each band, which were analyzed using `AstroImageJ` (Collins et al. 2017) with the best rms = 0.004 mag precision.

3.3. Ground-based Follow-up Spectroscopic Observation

3.3.1. Xinglong Observatory

From 2021 to 2022, we acquired 14 high-resolution spectra of TOI-1251 B on five separate nights by using the fiber-fed High Resolution Spectrograph (HRS) (Fan et al. 2016) mounted on the Xinglong 2.16 m telescope. The HRS is a high-resolution echelle spectrograph, equipped with an astro-comb (Zhao et al. 2019) for high precision wavelength

Table 4
Ground-based Photometric Follow-up Observation of TOI-1251 B

Date	Telescope	Band	Duration (minutes)	Number of Images
2019/10/12	AUKR 0.8 m	*R*	315	1267
2019/10/18	TCS 1.52 m	SDSS $g'r'i'z'$	77.2	3060
2020/04/02	Xinglong 0.6 m	*BVRI*	257	807
2020/08/17	AUKR 0.8 m	SDSS g', z'	363	706
2021/08/28	Xinglong 0.85 m	*BVRI*	243	845
				Total images: 6685

calibration, a resolution $R = 49{,}000$ and a spectral range spanning 360–1000 nm. While ensuring time resolution, we aimed to optimize the exposure time to acquire data with high S/Ns. Therefore, a single exposure does not need to exceed 1800 s for targets brighter than $V = 11.5$. We used spectra in 600–700 nm to determine radial velocities (RVs), and with exposure time of 1800 s we yielded S/Ns in 28–33 pixel^{-1} in this wavelength range. All spectra were exposed with simultaneous calibration fibers so that calibration spectra were simultaneously obtained with the target in one image to reduce any potential casual error between different images.

3.3.2. Roque De Los Muchachos Observatory (ORM)

We conducted observations of TOI-1251 B using the high-resolution FIbre-fed Echelle Spectrograph (FIES) (Telting et al. 2014) instrument mounted on the Nordic Optical Telescope (NOT, 2.56 m) located at ORM, La Palma, Spain (Djupvik & Andersen 2010). FIES is a cross-dispersed high-resolution echelle spectrograph that employs two fibers simultaneously feeding the spectrograph. The entire spectral range covers 376–884 nm, with our spectra obtained in HIGH-RES mode where $R = 67{,}000$. We used the wavelength range from approximately 400–550 nm to determine the RVs. The exposure time was approximately 1200 s yielding an S/N in 30–40 pixel^{-1} in the wavelength range used. From 2020 June 26th to October 11th, we obtained 12 spectra of TOI-1251 B totally.

3.3.3. FLWO

We utilized the Tillinghast Reflector Echelle Spectrograph (TRES) (Fürész 2008) mounted on the 1.5 m Tillinghast Reflector telescope at FLWO to observe both TOI-1194 b and TOI-1251 B. The TRES visible range covers 385–909 nm at a resolution of $R = 44{,}000$. From 2019 December 12th–13th, and 2023 February 5th–26th, we acquired twelve spectra of TOI-1194 b with exposure times ranging from 650 s to 2000 s, and S/N of approximately 30 pixel^{-1}. For TOI-1251 B, we obtained two spectra with exposure times of 1500 s (S/N $\sim$ 40 pixel^{-1}) and 900 s (S/N $\sim$ 33 pixel^{-1}), respectively, on 2019 October 20th and 23rd.

4. Photometric Data Analysis

4.1. Data Reduction Pipeline: QLCP

Following the acquisition of observation follow-up data, we performed data reduction and utilized it to identify the transit signals. To increase the sampling frequency of the key transit phase, such as ingress and egress, we shortened the exposure time of each image while ensuring a high S/N. We employed our Quick Light-Curve Pipeline (QLCP) (Zheng 2023), a Python-based pipeline. QLCP has the capability of performing differential photometry and generating light curves by aligning stars from a series of photometric images, along with conducting automated bias and flat corrections. Fluxes are calculated by default using `MAG_AUTO` of Source-Extractor (SExtractor, Bertin & Arnouts 1996), with the option of switching to alternative flux evaluation methods by adjusting the configuration. Field stars with stable fluxes will be identified by QLCP as reference stars, or they can be manually designated. The pipeline generates a list in both text and binary formats, along with locating charts and producing light curve figures for further analysis.

4.2. Creation of Light Curves

For follow-up photometric images of TOIs with TESS magnitudes between nine and twelve, at least five reference stars can be selected within a 30′ FoV, provided that the brightness difference between the reference stars and the target does not exceed two magnitudes. QLCP is capable of conducting high-precision differential photometry for reference stars with S/Ns close to 100 despite significant difference in brightness, by utilizing adaptive aperture photometry in SExtractor (Bertin & Arnouts 1996). Therefore, it is very suitable for processing the transit data of TOIs brighter than 8 mag which were observed according to the strategy described in Section 2.1. We use QLCP to quickly generate light curves after the completion of the data reduction and differential photometry. This process is interactive, making it intuitive for choosing reference stars.

4.3. Planet Transit Model Fitting

We performed data fitting of transit data using the `EXOFASTv2` online service, supported by the NASA Exoplanet

Table 5
The Prior Distribution of Transit-only Fit

Parameter	Description(Unit)	TOI-1194	TOI-1251
[Fe/H]	Metallicity (dex)[a]	$\mathcal{N}(0.28, 0.05)$	$\mathcal{N}(-0.24, 0.05)$
$T_{\rm eff}$	Effective temperature (K)[a]	$\mathcal{N}(5553.93, 140)$	$\mathcal{N}(6038.91, 140.00)$
log(g)	Surface gravity (cgs)[a]	$\mathcal{N}(4.5, 0.1)$	$\mathcal{N}(4.2, 0.1)$
T_c	Time of conjunction (BJD_{TDB})[b]	$\mathcal{N}(2459632.287997, 0.0001554)$	$\mathcal{N}(2459759.178675, 0.0001791)$
R_p/R_*	Ratio of Planet to Stellar Radius	$\mathcal{N}(0.1, 0.05)$	$\mathcal{N}(0.006, 0.003)$
i	Inclination (degree)	$\mathcal{N}(90, 20)$	$\mathcal{N}(90, 20)$
P	Planetary orbital period (days)[b]	$\mathcal{N}(2.3106444, 0.0000007)$	$\mathcal{N}(5.9630544, 0.0000015)$

Notes.
[a] Starhorse (Anders et al. 2019, 2022).
[b] ExoFOP-TESS, https://exofop.ipac.caltech.edu/tess/.

Science Institute (Eastman et al. 2013; Eastman 2017). In order to efficiently identify potential planets from a vast amount of observed TOI transit data, we initially visually detected distinguishable transits after generating light curves and prioritized multiband light curve fitting for these targets. However, for TOIs with transit depths below the photometry accuracy threshold, their transits necessitate phase folding in an attempt to uncover the transit signal. Following data reduction and flux normalization, we input each band transit photometric data and prior distribution of parameters (see Table 5) into `EXOFASTv2`, which employs Markov chain Monte Carlo (MCMC) analysis to perform model fitting and parameter analysis of both the host star and planet. The convergence criteria for MCMC independent sampling here are described in Eastman et al. (2013).

5. Verification

5.1. Multiband Light Curve Fitting

Comparative analysis of multiband light curves is the core of planet identification in this work. Prior to this work, detailed stellar parameters were lacking for both the host stars of TOI-1194 b and TOI-1251 B, and were therefore supplemented based on the analysis of transit photometric data and high-resolution spectra. The best-fit models for the two targets were obtained by reducing and analyzing TOI-1194 observation data obtained on 2022 February 21st and TOI-1251 observation data obtained on 2021 August 28th. Remaining observation data were fitted using these best-fit models (see Figures 2 and 3). The transit depth (δ) and limb-darkening coefficients (u_1, u_2) obtained by fitting the transit light curve of each band are shown in Table 6. Both candidates are achromatic in the measurement accuracy of better than 1%.

5.2. Radial Velocity Fitting

Determining the mass of the companions enables direct confirmation of their planetary status. To accomplish this, we reduced the high-resolution spectra of TOI-1194 and TOI-1251 captured by the TRES, FIES and HRS instruments, calculated their RVs and derived their phase-RV variation curves, before analyzing their orbital solutions. Reduction and multi-order spectrum analysis from TRES and FIES were conducted using the method described in Buchhave et al. (2010). We utilized the Stellar Parameters Classification (SPC) tool to estimate the stellar parameters. The SPC tool relies on synthetic grid library spectra and simultaneously derives the effective temperature, surface gravity, metallicity and rotational velocity by matching the models with the observed spectra originating from different instruments (Buchhave et al. 2012, 2014). (The reference stellar atmospheric models are from Kurucz (1992).) High-resolution RV data obtained from follow-up observations by HRS were reduced using `GAMSE`[22] for one-dimensional spectral extraction from double-fiber high-resolution spectra. We employed `IRAF` to fit nine lines in Order93 and Order98 for calculating RV in 600–700 nm (Tody 1986). We utilized `barycorrpy` (Kanodia & Wright 2018) to calculate the barycentric RV correction. Three points of HRS RV data obtained on 2021 November 22nd were disregarded, due to poor S/Ns and insufficient identifiable lines. To enable fitting of all RV points collected from the three instruments, we shifted the systemic velocity (γ) of each instrument to 0 m s^{-1}. Table 7 shows RV data of TOI-1194 b, while Table 8 displays RV data of TOI-1251 B, within best models obtained when the χ^2/dof value is lowest.

We utilized both `EXOFASTv2` and `Exo-Striker` (Trifonov 2019) to fit RV points for two TOIs, with best-fitted models visualized in Figures 4 and 5. The calculated RV amplitude for TOI-1194 b is $K = 69.4^{+7.9}_{-7.3}$ m s^{-1}, with a derived minimum mass of $M_p \sin i = 0.453^{+0.055}_{-0.051} M_{\rm J}$, which appears close to Saturn in terms of mass and orbits its host star on a nearly circular orbit.

The RV amplitude of TOI-1251 is notably distinctly different from that of TOI-1194, due to the former being a very low-mass star. We calculate the RV amplitude caused by TOI-1251 B to be $K = 9849^{+42}_{-40}$ m s^{-1}, with a minimum mass of $M_2 \sin i = 96.3 \pm 1.5\, M_{\rm J}$. The fitted RV curve suggests that

[22] https://github.com/wangleon/gamse

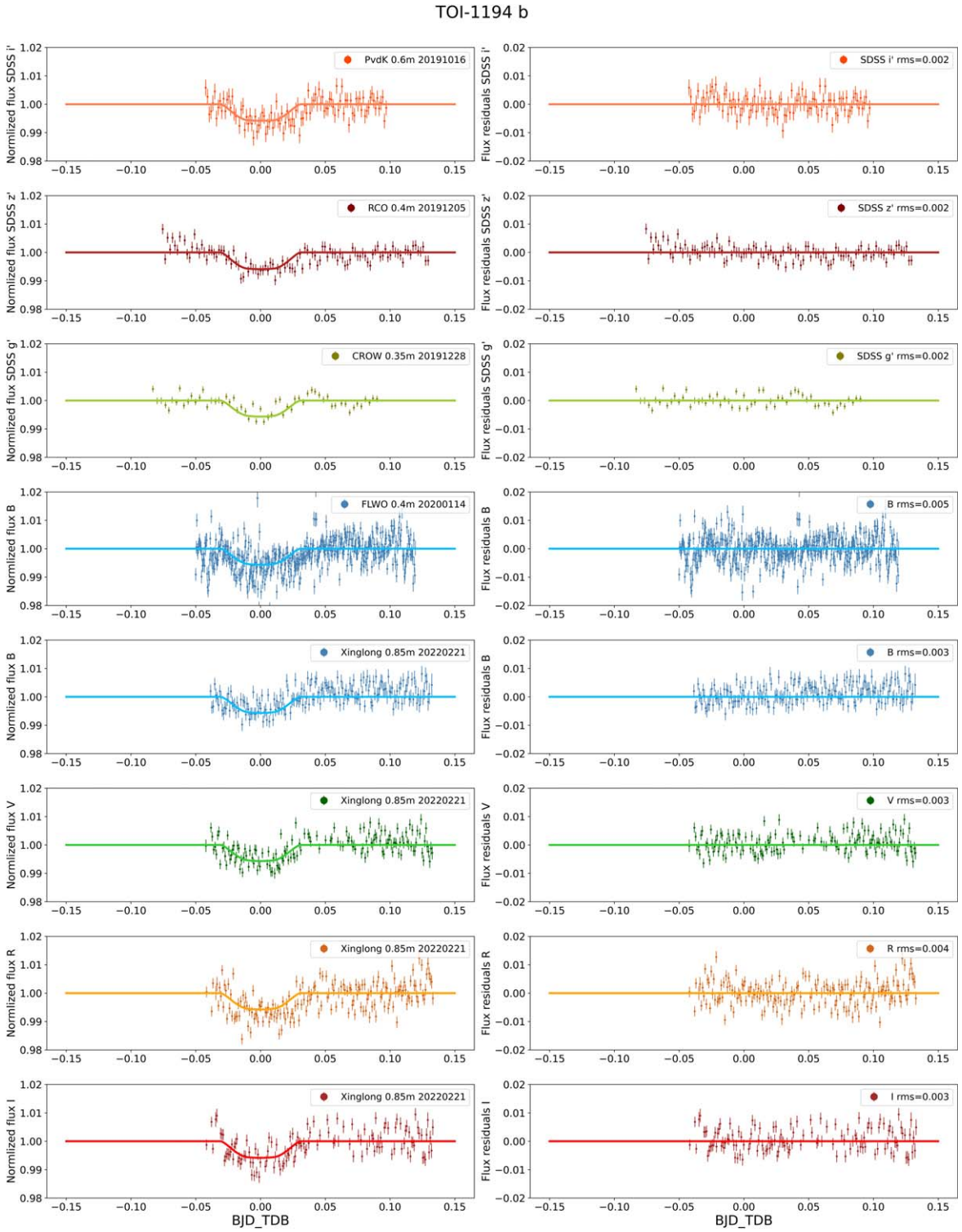

Figure 2. TOI-1194 b multiband light curves with fitting models.

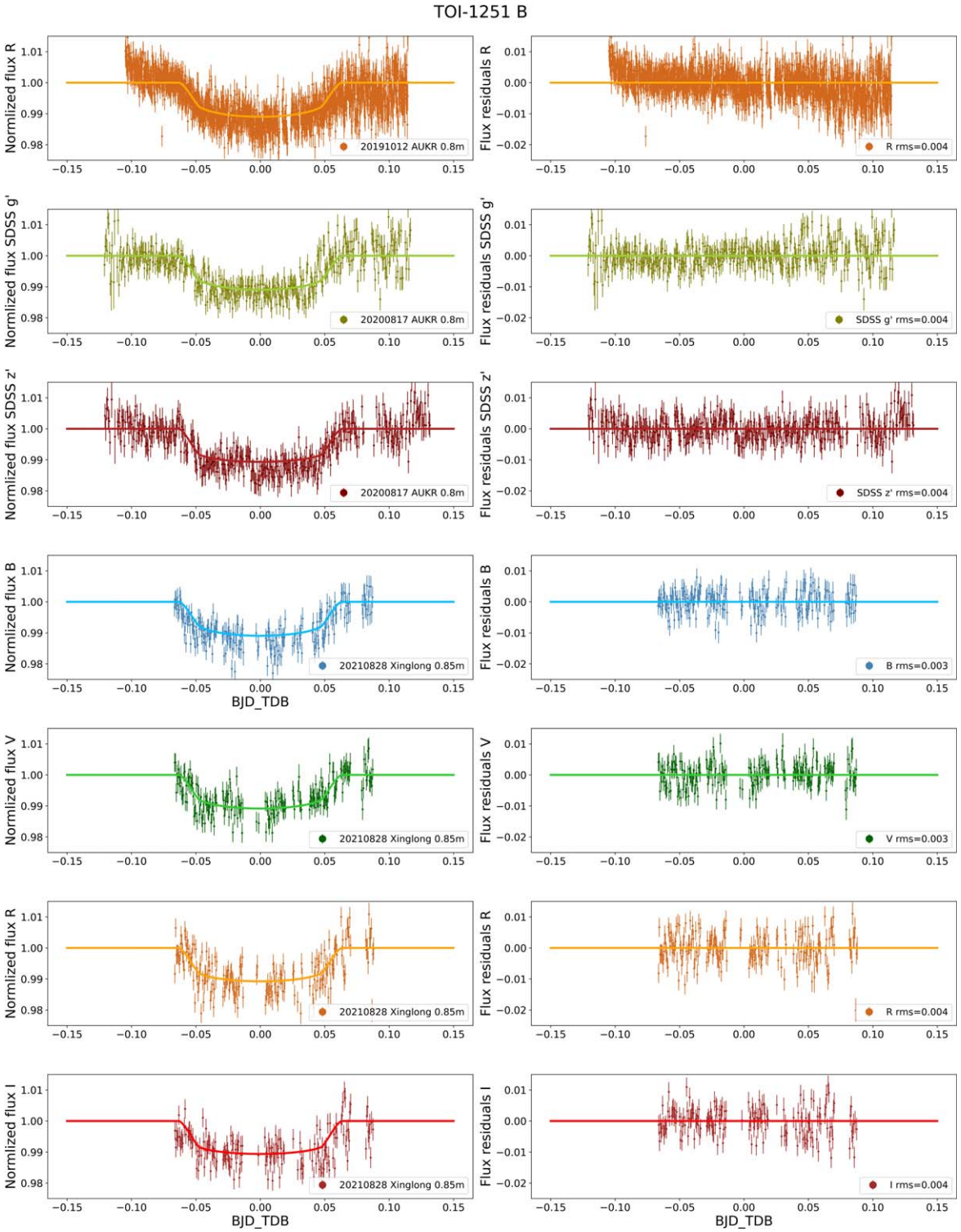

Figure 3. TOI-1251 B multiband light curves with fitting models.

Table 6
Fitted Transit Depth and Limb-darkening Coefficient of Each Band

Parameter	Description (Unit)	TOI-1194	TOI-1251
Transit Depth			
δ_B	Transit depth of Johnson-Cousins B band (ppm)	6684^{+80}_{-79}	9975^{+358}_{-356}
δ_V	Transit depth of Johnson-Cousins V band (ppm)	6694^{+82}_{-81}	9759^{+349}_{-349}
δ_R	Transit depth of Johnson-Cousins R band (ppm)	6700^{+81}_{-80}	10370^{+291}_{-293}
δ_I	Transit depth of Johnson-Cousins I band (ppm)	6701^{+78}_{-79}	9620^{+354}_{-351}
$\delta_{g'}$	Transit depth of SDSS g' band (ppm)	6691^{+80}_{-79}	10178^{+321}_{-328}
$\delta_{r'}$	Transit depth of SDSS r' band (ppm)	...	10017^{+370}_{-356}
$\delta_{i'}$	Transit depth of SDSS i' band (ppm)	6693^{+82}_{-79}	9804^{+395}_{-388}
$\delta_{z'}$	Transit depth of SDSS z' band (ppm)	6690 ± 80	10748^{+306}_{-304}
Limb-darkening Coefficient			
$u_1(B)$	Linear limb-darkening coeff of Johnson-Cousins B band	0.781 ± 0.051	$0.667^{+0.050}_{-0.051}$
$u_2(B)$	Quadratic limb-darkening coeff of Johnson-Cousins B band	0.061 ± 0.050	0.158 ± 0.050
$u_1(V)$	Linear limb-darkening coeff of Johnson-Cousins V band	$0.563^{+0.051}_{-0.052}$	0.459 ± 0.051
$u_2(V)$	Quadratic limb-darkening coeff of Johnson-Cousins V band	0.192 ± 0.050	$0.256^{+0.050}_{-0.049}$
$u_1(R)$	Linear limb-darkening coeff of Johnson-Cousins R band	$0.450^{+0.050}_{-0.052}$	$0.370^{+0.051}_{-0.049}$
$u_2(R)$	Quadratic limb-darkening coeff of Johnson-Cousins R band	$0.231^{+0.051}_{-0.049}$	$0.282^{+0.048}_{-0.050}$
$u_1(I)$	Linear limb-darkening coeff of Johnson-Cousins I band	$0.349^{+0.051}_{-0.050}$	$0.278^{+0.049}_{-0.050}$
$u_2(I)$	Quadratic limb-darkening coeff of Johnson-Cousins I band	$0.247^{+0.050}_{-0.049}$	$0.268^{+0.051}_{-0.049}$
$u_1(g')$	Linear limb-darkening coeff of SDSS g' band	0.696 ± 0.051	0.585 ± 0.051
$u_2(g')$	Quadratic limb-darkening coeff of SDSS g' band	0.119 ± 0.051	0.221 ± 0.050
$u_1(r')$	Linear limb-darkening coeff of SDSS r' band	...	$0.386^{+0.049}_{-0.051}$
$u_2(r')$	Quadratic limb-darkening coeff of SDSS r' band	...	$0.277^{+0.051}_{-0.050}$
$u_1(i')$	Linear limb-darkening coeff of SDSS i' band	0.377 ± 0.050	0.316 ± 0.050
$u_2(i')$	Quadratic limb-darkening coeff of SDSS i' band	0.246 ± 0.050	$0.282^{+0.050}_{-0.051}$
$u_1(z')$	Linear limb-darkening coeff of SDSS z' band	0.304 ± 0.050	$0.273^{+0.050}_{-0.051}$
$u_2(z')$	Quadratic limb-darkening coeff of SDSS z' band	0.254 ± 0.050	$0.291^{+0.049}_{-0.050}$

TOI-1251 B orbits its host star on a nearly circular orbit, consistent with parameters obtained in fitted light curves.

5.3. Joint Analysis

The parameters of TOI-1194 b and TOI-1251 B were derived through a joint analysis of all available ground-based photometric and spectroscopic data. We employed Exo-Striker to conduct the joint MCMC analysis (Foreman-Mackey et al. 2013), initializing 20 walkers and generating 2000 steps for the burn-in phase, and a further 10,000 steps to sample the posterior parameter distribution of stellar and planetary parameters from the MCMC process.

In addition to the transit epoch (T_c) and period (P) in Table 5, the prior parameters used also include metallicity ([Fe/H]), surface gravity (log g) and effective temperature ($T_{\rm eff}$), which were obtained by fitting stellar spectra (Section 5.2). Since planets appear to be in nearly circular orbits based on the RV curve fitting, we assigned a Gaussian distribution $\mathcal{N}(0, 0.1)$ as a prior.

The process ultimately converged to the maximum likelihood estimate. The joint analysis results, presented at the 1σ confidence interval in Tables 9 and 10, indicate that the mass of TOI-1194 b is $0.456^{+0.055}_{-0.051}\,M_{\rm J}$, while the mass of TOI-1251 B is $96.5 \pm 1.5\,M_{\rm J}$.

Table 7
Ground-based Follow-up Radial Velocities for TOI-1194 b

$\rm BJD_{TDB}$	RV ($\rm m\,s^{-1}$)	$e_{\rm RV}$ ($\rm m\,s^{-1}$)	Instrument
2458829.952974	129.80	20.77	FLWO 1.5 m TRES
2458830.979613	−47.76	22.29	FLWO 1.5 m TRES
2459980.881301	30.22	20.77	FLWO 1.5 m TRES
2459981.855344	−38.24	25.88	FLWO 1.5 m TRES
2459982.837025	46.81	23.01	FLWO 1.5 m TRES
2459983.853953	−91.88	19.20	FLWO 1.5 m TRES
2459984.855371	60.96	17.91	FLWO 1.5 m TRES
2459985.938541	−0.69	16.18	FLWO 1.5 m TRES
2459987.909966	−3.17	17.74	FLWO 1.5 m TRES
2459991.837408	40.57	21.77	FLWO 1.5 m TRES
2460000.815599	−43.86	21.72	FLWO 1.5 m TRES
2460001.824999	32.74	24.48	FLWO 1.5 m TRES

5.4. Potential Contamination

Apart from the EBs mentioned in Section 1, the eclipses of nearby EBs are usually responsible for the high FP probability in exoplanet surveys as well. Approximately half of all discovered planets orbit stars with stellar companions (Howell et al. 2021;

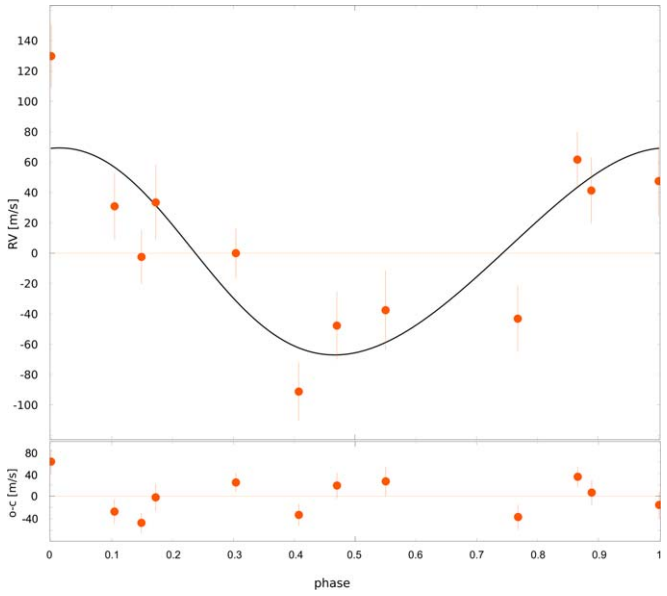

Figure 4. The fitted RV curve of TOI-1194 b by follow-up high resolution spectra.

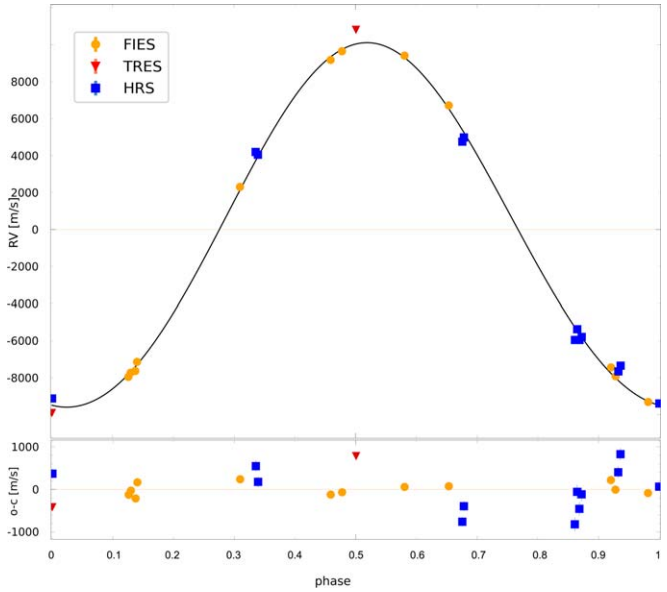

Figure 5. The fitted RV curve of TOI-1251 B by follow-up high resolution spectra.

Lester et al. 2021a). However, follow-up photometric data and Gaia DR3 catalogs alone are not sufficient to distinguish such companions in regions between 10 and 100 au around the host stars. High-resolution imaging data have the potential to exclude some companions around the host stars (Lester et al. 2021b). The resolution of ground-based optical telescopes without adaptive optics depends on the atmosphere seeing conditions. At

Table 8
Ground-based Follow-up Radial Velocities for TOI-1251 B

BJD_{TDB}	RV ($m\,s^{-1}$)	e_{RV} ($m\,s^{-1}$)	Instrument
2458776.68854	−10363.24	67.18	FLWO 1.5 m TRES
2458779.66325	10356.45	67.18	FLWO 1.5 m TRES
2459026.64331	−7527.15	67.48	NOT 2.56 m FIES
2459036.54954	9326.95	91.73	NOT 2.56 m FIES
2459038.61436	−8007.87	53.32	NOT 2.56 m FIES
2459093.47847	−8041.56	108.67	NOT 2.56 m FIES
2459093.50021	−7818.58	79.84	NOT 2.56 m FIES
2459095.45703	9096.31	56.86	NOT 2.56 m FIES
2459105.47225	−7720.50	72.90	NOT 2.56 m FIES
2459119.42068	9566.68	62.45	NOT 2.56 m FIES
2459123.37912	−7229.17	83.26	NOT 2.56 m FIES
2459124.38530	2216.98	98.45	NOT 2.56 m FIES
2459132.39111	6631.18	52.06	NOT 2.56 m FIES
2459134.34215	−9398.61	50.26	NOT 2.56 m FIES
2459539.93873	−9629.71	107.67	Xinglong 2.16 m HRS
2459539.96100	−9357.86	107.67	Xinglong 2.16 m HRS
2459631.39846	3962.04	126.91	Xinglong 2.16 m HRS
2459631.42052	3814.53	126.91	Xinglong 2.16 m HRS
2459639.38316	4519.53	116.19	Xinglong 2.16 m HRS
2459639.39846	4748.09	116.19	Xinglong 2.16 m HRS
2459754.20779	−7892.08	135.92	Xinglong 2.16 m HRS
2459754.22996	−7582.42	135.92	Xinglong 2.16 m HRS
2459890.93302	−6189.59	158.63	Xinglong 2.16 m HRS
2459890.95543	−5610.81	158.63	Xinglong 2.16 m HRS
2459890.97752	−6190.05	158.63	Xinglong 2.16 m HRS
2459890.99957	−6025.26	158.63	Xinglong 2.16 m HRS

Xinglong Observatory, the median seeing value is around 1.″7 (Zhang et al. 2015), incapable of ruling out stellar contaminations from stars present in this sky region via aperture photometry alone. We used the 'Alopeke instrument on the Gemini North 8 m telescope to observe TOI-1194 on 2020 February 17th and obtained high-resolution speckle images in the 562 and 716 nm bands to search for nearby stellar companions (see Figure 6). The data were reduced using the standard speckle interferometry pipeline as described in Howell et al. (2011). From the 5σ contrast curves shown in Figure. 6, we found that within the angular and magnitude limits achieved, there is no close companion star within 5–7 mag and between 0.″02 (the diffraction limit of the device) and 1″. These angular limits correspond to 2.96–148 au around TOI-1194, which is located 148 pc away.

The 562 and 832 nm speckle images of TOI-1251 from the WIYN telescope revealed the presence of a star located 0.″22 away from the host star (equivalent to a projected separation of about 41 au), with Δmag = 1.66 in the 562 nm band and Δmag = 1.36 in the 832 nm band (Howell et al. 2021). However, from follow-up photometric and spectroscopic RV data, we discerned the existence of only one stellar companion, which orbits the host star in a nearly circular orbit with a

Table 9
TOI-1194 Host Stellar and Planetary Parameters at 68% Confidence Intervals

Parameter	Description (Units)	Value
Host Stellar Parameters		
R.A.	R.A. coordinate (J2000.0)[a]	$11^{h}11^{m}16\overset{s}{.}91$
Decl.	Decl. coordinate (J2000.0)[a]	$+69^{d}57^{m}52\overset{s}{.}94$
B [mag]	Johnson-Cousins B band magnitude[b]	11.833 ± 0.081
V [mag]	Johnson-Cousins V band magnitude[c]	11.185 ± 0.042
G [mag]	Gaia G band magnitude[d]	10.9887 ± 0.0004
I [mag]	Johnson-Cousins I band magnitude[c]	10.289 ± 0.020
M_*	Mass ($M_\odot$)	$1.007^{+0.050}_{-0.048}$
R_*	Radius ($R_\odot$)	$0.963^{+0.056}_{-0.051}$
L_*	Luminosity ($L_\odot$)	$0.732^{+0.095}_{-0.081}$
ρ_*	Density (cgs)	$1.59^{+0.26}_{-0.22}$
$\log g$	Surface gravity (cgs)	$4.473^{+0.043}_{-0.042}$
$T_{\rm TIC}$	Effective Temperature from TIC (K)[e]	$5323.0^{+92.9}_{-156.1}$
$T_{\rm Gaia}$	Effective Temperature from Gaia (K)[d]	$5339.90^{+207.10}_{-116.23}$
$T_{\rm eff}$	Best fitting Effective Temperature (K)	5446^{+51}_{-48}
[Fe/H]	Metallicity (dex)	0.290 ± 0.078
vsini	Minimum rotational velocity (km s^{-1})	2.4 ± 0.5
ϖ	Parallax (mas)[a]	6.6527 ± 0.0126
d	Distance (kpc)[a]	$0.148508^{+0.003023}_{-0.003278}$
Planetary Companion Parameters		TOI-1194 b
P	Period (days)	2.310644 ± 0.000001
R_P	Radius (R_J)	$0.767^{+0.045}_{-0.041}$
M_P	Mass (M_J)	$0.456^{+0.055}_{-0.051}$
ρ_P	Density (cgs)	$1.25^{+0.26}_{-0.21}$
$\log(g_p)$	Surface gravity	3.281 ± 0.064
M_P/M_*	Mass ratio	$0.000432^{+0.000050}_{-0.000046}$
R_P/R_*	Radius of planet in stellar radii	0.08196 ± 0.00047
a/R_*	Semi-Major Axis in stellar radii	$7.65^{+0.39}_{-0.37}$
δ	Transit depth (fraction)	0.006717 ± 0.000078
K	RV Semi-Amplitude (m s^{-1})	$69.4^{+7.9}_{-7.3}$
T_0	Time of conjunction (BJD$_{\rm TDB}$)	$2459632.28801 \pm 0.00015$
a	Semimajor axis (au)	0.03428 ± 0.00055
i	Inclination (Degrees)	83.98 ± 0.50
b	Transit Impact parameter	$0.802^{+0.025}_{-0.027}$
e	Eccentricity	$0.076^{+0.032}_{-0.043}$
ω	Argument of Periastron (Degree)	$76.7^{+49.7}_{-39.5}$
T_{14}	Total transit duration (hours)	$1.684^{+0.063}_{-0.058}$
$T_{\rm eq}$	Equilibrium temperature (K)	1391^{+38}_{-37}
$\chi^2_{\rm RV}$	RV fitting χ^2 value	3.89
rms$_{\rm RV}$	RV fitting rms value (m s^{-1})	31.8

Notes.
[a] Gaia DR3.
[b] All-sky compiled catalog of 2.5 million stars (ASCC-2.5 V3) (Kharchenko 2001).
[c] TASS Mark IV Photometric Survey of the Northern Sky (Droege et al. 2006).
[d] Gaia DR2 (Gaia Collaboration 2018).
[e] TIC v8.2 (Paegert et al. 2021).

Table 10
TOI-1251 Host and Companion Stellar Parameters at 68% Confidence Intervals

Parameter	Description (Units)	Value
Host Stellar Parameters		
R.A.	R.A. coordinate (J2000.0)[a]	$18^{h}14^{m}07\overset{s}{.}07$
Decl.	Decl. coordinate (J2000.0)[a]	$+62^{d}51^{m}29\overset{s}{.}71$
B [mag]	Johnson-Cousins B band magnitude[b]	12.020 ± 0.127
V [mag]	Johnson-Cousins V band magnitude[c]	11.318 ± 0.037
G [mag]	Gaia G band magnitude[d]	11.0942 ± 0.0010
I [mag]	Johnson-Cousins I band magnitude[c]	10.505 ± 0.021
M_*	Mass ($M_\odot$)	$1.057^{+0.050}_{-0.049}$
R_*	Radius ($R_\odot$)	$0.986^{+0.025}_{-0.024}$
L_*	Luminosity ($L_\odot$)	$0.968^{+0.066}_{-0.062}$
ρ_*	Density (cgs)	$1.553^{+0.061}_{-0.059}$
$\log g$	Surface gravity (cgs)	$4.4737^{+0.0096}_{-0.0093}$
$T_{\rm Gaia}$	Effective Temperature from Gaia (K)[d]	$5759.71^{+163.69}_{-209.53}$
$T_{\rm eff}$	Best fitting Effective Temperature (K)	5769^{+49}_{-50}
[Fe/H]	Metallicity (dex)	0.019 ± 0.080
vsini	Minimum rotational velocity (km s^{-1})	9.2 ± 0.5
ϖ	Parallax (mas)[a]	3.6550 ± 0.3382
d	Distance (kpc)[a]	$0.246147^{+0.010750}_{-0.011126}$
Companion Stellar Parameters		TOI-1251 B
P	Period (days)	5.963054 ± 0.000001
R_2	Radius (R_J)	$0.947^{+0.037}_{-0.035}$
M_2	Mass (M_J)	$96.47^{+1.50}_{-1.47}$
ρ_2	Density (cgs)	141^{+13}_{-12}
$\log(g_2)$	Surface gravity	$5.425^{+0.024}_{-0.025}$
M_2/M_*	Mass ratio	$0.0876^{+0.0007}_{-0.0008}$
R_2/R_*	Radius of planet in stellar radii	0.0987 ± 0.0022
a/R_*	Semi-Major Axis in stellar radii	14.69 ± 0.19
δ	Transit depth (fraction)	$0.00975^{+0.00043}_{-0.00042}$
K	RV Semi-Amplitude (m s^{-1})	9849^{+42}_{-40}
T_0	Time of conjunction (BJD$_{\rm TDB}$)	$2459759.17874^{+0.00017}_{-0.00018}$
a	Semimajor axis (au)	0.0674 ± 0.0010
i	Inclination (Degrees)	$92.3^{+0.08}_{-0.11}$
b	Transit Impact parameter	$0.469^{+0.027}_{-0.030}$
e	Eccentricity	$0.028^{+0.002}_{-0.001}$
ω	Argument of Periastron (Degree)	341^{+6}_{-5}
T_{14}	Total transit duration (hours)	$3.086^{+0.041}_{-0.040}$
$\chi^2_{\rm RV}$	RV fitting χ^2 value	3.37
rms$_{\rm RV}$	RV fitting rms value (m s^{-1})	390.7

Notes.
[a] Gaia DR3.
[b] All-sky compiled catalog of 2.5 million stars (ASCC-2.5 V3) (Kharchenko 2001).
[c] TASS Mark IV Photometric Survey of the Northern Sky (Droege et al. 2006).
[d] Gaia DR2 (Gaia Collaboration 2018).

semimajor axis of $a = 0.0674 \pm 0.0010$ au. While the angular separation between the companion and the host star observed from the Earth's perspective is $0\overset{''}{.}0002$, high-resolution imaging cannot currently observe it. This in turn indicates that the star located within 41 au of the host star is not dynamically associated with it.

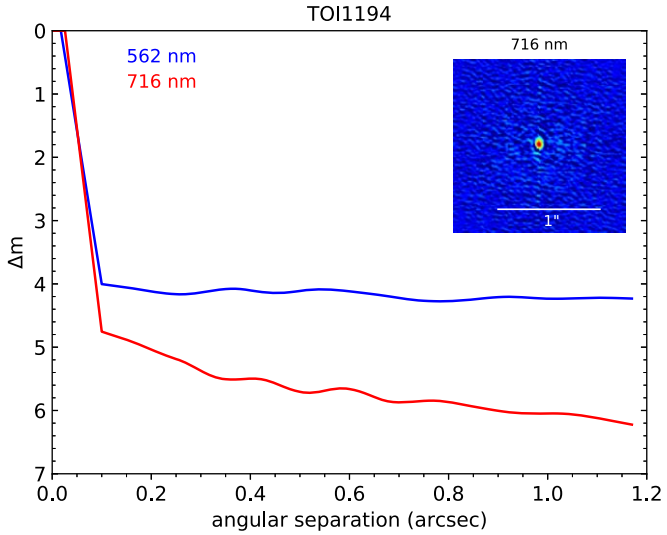

Figure 6. The blue and red curves show the 5σ contrast sensitivity limits in 562 and 716 nm respectively of TOI-1194. The observations were obtained using the 'Alopeke instrument on the Gemini North telescope. The upper right inset shows the reconstructed 716 nm speckle image.

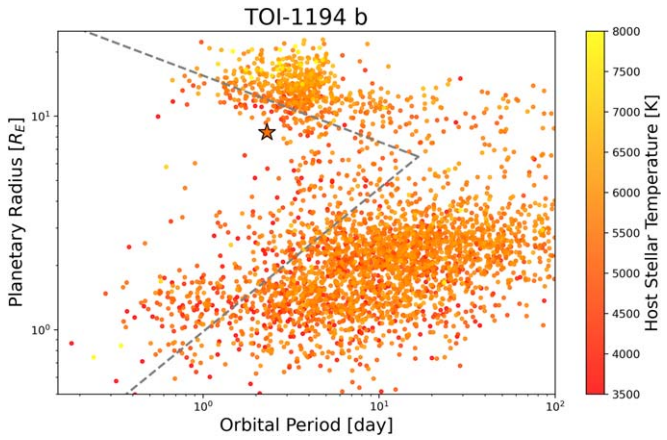

Figure 7. The period–radius diagram of confirmed planets; gray dashed lines are the region of the Neptune desert described in Mazeh et al. (2016).

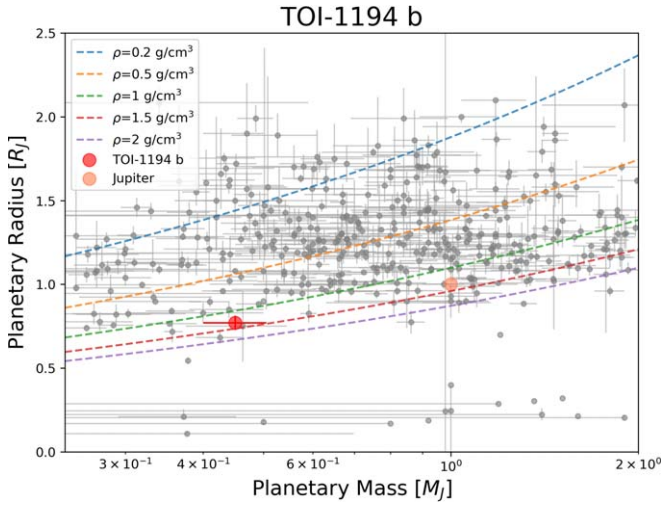

Figure 8. The mass–radius diagram of confirmed hot Jupiters ($M_P \geqslant 0.25\ M_J$, $P \leqslant 10$ days) with mass $\leqslant 2\ M_J$; the red point is TOI-1194 b, the yellow point is Jupiter and dashed lines with different colors correspond to the density values shown in the legend. The density of TOI-1194 b is close to that of Jupiter and is relatively dense among these hot Jupiter shown here.

6. Summary and Discussion

In our efforts to follow-up on TOIs, we organized a Sino-German campaign group that collected multiple transit photometric data observed in multiband to validate them as planets. The first three years of observation and current data analysis demonstrate that the one meter-class telescopes in our campaign can provide valuable transit and RV data for the identification and planetary property analysis of TESS candidates. Through processing and fitting of these data, we confirmed the presence of a planet, TOI-1194 b, and a very low-mass star, TOI-1251 B, each orbiting G-type hosts. Identifying a planet using only single-band photometric observations collected over a long time baseline is quite difficult due to differences in transit depth across multiband light curves displayed by EBs. In addition to improving observational accuracy and increasing transit data availability, multiband simultaneous photometric observation data are also helpful for the rapid elimination of FP caused by EBs. Moreover, one meter-class telescopes are more accessible and offer cheaper observational resources compared to spectral observation equipment. The ability to conduct multiband photometric observation of exoplanets through a multi-site campaign can also enable faster response times and feedback on follow-up observation results for candidates detected through space-based observations like TESS, enhancing the efficiency and accuracy of exoplanet confirmation.

TOI-1194 b has a density of $\rho = 1.25^{+0.26}_{-0.21}$ g cm^{-3}, suggesting that this hot Saturn is comparable in density to Jupiter and is located in the Neptune desert described in Mazeh et al. (2016) (see Figure 7). Figure 8 illustrates the mass–radius diagram of confirmed hot Jupiters with mass under 2 M_J, with TOI-1194 falling into a relatively dense and sparsely populated region (Espinoza et al. 2017). As statistics on ultra-short period planet (USP) samples and the evolution model of hot gas giant planets, it is hypothesized that planets with this nature, exposed to strong ultraviolet and thermal radiation from their host stars, may experience expansion and gradual loss of their outer envelope over time (Owen & Wu 2013). The radial expansion of the planet also increases with enhanced radiation from the host star, and this radiation-induced inflation mechanism is evident at $T_{\rm eq} \geqslant 1000$ K (Demory & Seager 2011). The $T_{\rm eq}$ of TOI-1194 b is ~1400 K, but the radius does not show a significant expansion effect, so it is relatively dense. The higher density of TOI-1194 b may be attributed to its higher proportion of heavy elements (Miller & Fortney 2011), and the relationship between planet

and metal-rich host star may be reasonably explained by protoplanetary disk evolution theories.

TOI-1251 B is an M-dwarf and is located remarkably close to its host star, with an extremely low mass ratio $q = M_2/M^* = 0.088$, but positioned outside the Roche limit (0.00025 au). M dwarfs are widely distributed in the universe. Due to the smaller radius and mass of M dwarfs, the transit depth and RV variation caused by smaller planets (such as Neptune and Earth-like planets) are more pronounced than those around Sun-like stars (Tuomi et al. 2019), and these small planets are more likely to be detected by one meter-class telescope, so they have attracted much attention in recent years. The statistical results demonstrate a significantly high occurrence rate of low-mass planets around M dwarfs, with a correspondingly high likelihood of super-Earths (3–10$M_\oplus$) existing within their habitable zones (Tuomi et al. 2014; Dressing & Charbonneau 2015). Although most M-dwarfs identified in EB systems exhibit mass similar to that of another star in the system, there are fewer than 100 M-dwarfs orbiting F/G/K-type stars known with an extremely low mass ratio ($q \leqslant 0.15$) (Grieves et al. 2021). Due to the limited sample, the origin and evolution of these EBs lack a systematic explanation. TOI-1251 B expands the sample as a new eclipsing binary with low-mass (EBLM), with the period obtained from this work being consistent with that provided within the Gaia DR3 non-single stars catalog. This consistency indicates that it is a single-lined spectroscopic binary (SB) (Gaia Collaboration 2022). Direct observations of very low mass stars are challenging due to their low surface luminosity compared to massive stars. Nonetheless, the methods employed in exoplanet follow-up observation are well-suited to the observation of these types of stars. Therefore, identifying new EBLMs in TOI candidates using follow-up photometric and spectroscopic observations may become easier.

Acknowledgments

We thank Dr. David W. Latham and the TRES team for providing the TRES results and helpful suggestions that improved the manuscript. This work is supported by National Natural Science Foundation of China (NSFC, Grant Nos. U1831209 and U2031144) and the research fund of Ankara University (BAP) through the project 18A0759001. This paper refers to some data which are publicly available from the Mikulski Archive for Space Telescopes (MAST), collected by the TESS mission. The TESS mission is funded by NASA's Science Mission directorate. We acknowledge the TESS Follow-up Observing Program (TFOP) SG1, SG2, SG3 and SG4 for the disposition of candidates, and the use of public TOI Release data from pipelines at the TESS Science Office (TSO) and at the TESS Science Processing Operations Center. Resources supporting this work were provided by the NASA High-End Computing (HEC) Program through the NASA Advanced Supercomputing (NAS) Division at Ames Research Center for the production of the SPOC data products. This research has made use of data obtained from the portal exoplanet.eu of The Extrasolar Planets Encyclopaedia. This research has made use of the NASA Exoplanet Archive, which is operated by the California Institute of Technology, under contract with the National Aeronautics and Space Administration under the Exoplanet Exploration Program.

This article is partly based on observations made with the FLWO/TRES, NOT/FIES and MuSCAT2. We acknowledge the support of the staff of the Xinglong 60 cm, 80 cm, 85 cm and 2.16 m telescopes. This work was partially supported by the Open Project Program of the CAS Key Laboratory of Optical Astronomy, National Astronomical Observatories, Chinese Academy of Sciences. We acknowledge the support of the staff of Qingdao Aishan Observatory, Nanshan Observatory, Weihai Observatory, Skyline Observatory, Muztaga Observatory, Lijiang Gemini Observatory and Xingming Observatory. Some of the observations in this paper made use of the High-Resolution Imaging instrument 'Alopeke and were obtained under Gemini LLP Proposal Number: GN/S-2021A-LP-105. 'Alopeke was funded by the NASA Exoplanet Exploration Program and built at the NASA Ames Research Center by Steve B. Howell, Nic Scott, Elliott P. Horch, and Emmett Quigley. 'Alopeke was mounted on the Gemini North telescope of the international Gemini Observatory, a program of NSF's OIR Lab, which is managed by the Association of Universities for Research in Astronomy (AURA) under a cooperative agreement with the National Science Foundation, on behalf of the Gemini partnership: the National Science Foundation (United States), National Research Council (Canada), Agencia Nacional de Investigación y Desarrollo (Chile), Ministerio de Ciencia, Tecnología e Innovación (Argentina), Ministério da Ciência, Tecnologia, Inovções e Comunicações (Brazil), and Korea Astronomy and Space Science Institute (Republic of Korea).

This work made use of Astropy[23]: a community-developed core Python package and an ecosystem of tools and resources for astronomy (Astropy Collaboration et al. 2013, 2018, 2022). This work made use of Matplotlib (Hunter 2007), Numpy (van der Walt et al. 2011), PyEphem and PyTransit (Parviainen 2015). This work has made use of data from the European Space Agency (ESA) mission Gaia (https://www.cosmos.esa.int/gaia), processed by the Gaia Data Processing and Analysis Consortium (DPAC, https://www.cosmos.esa.int/web/gaia/dpac/consortium). Funding for the DPAC has been provided by national institutions, in particular the institutions participating in the Gaia Multilateral Agreement.

This paper makes use of EXOFAST (Eastman et al. 2013) as provided by the NASA Exoplanet Archive, which is operated by the California Institute of Technology, under contract with the National Aeronautics and Space Administration under the Exoplanet Exploration Program.

[23] http://www.astropy.org

ORCID iDs

Jia-Qi Wang https://orcid.org/0000-0001-8665-4598
Jie Zheng https://orcid.org/0000-0001-6637-6973
Liang Wang https://orcid.org/0000-0003-3603-1901
Mesut Yilmaz https://orcid.org/0000-0002-3276-0704
Hui-Juan Wang https://orcid.org/0000-0003-3271-9709

References

Akeson, R. L., Chen, X., Ciardi, D., et al. 2013, PASP, 125, 989
Anders, F., Khalatyan, A., Chiappini, C., et al. 2019, A&A, 628, A94
Anders, F., Khalatyan, A., Queiroz, A. B. A., et al. 2022, A&A, 658, A91
Astropy Collaboration, Price-Whelan, A. M., Sipőcz, B. M., et al. 2018, AJ, 156, 123
Astropy Collaboration, Price-Whelan, A. M., Lim, P. L., et al. 2022, ApJ, 935, 167
Astropy Collaboration, Robitaille, T. P., Tollerud, E. J., et al. 2013, A&A, 558, A33
Bai, C.-H., Fu, J.-N., Li, T.-R., et al. 2018, RAA, 18, 107
Beatty, T. G., Pepper, J., Siverd, R. J., et al. 2012, ApJL, 756, L39
Bertin, E., & Arnouts, S. 1996, A&AS, 117, 393
Borucki, W. J., Koch, D., Basri, G., et al. 2010, Sci, 327, 977
Buchhave, L. A., Bizzarro, M., Latham, D. W., et al. 2014, Natur, 509, 593
Buchhave, L. A., Bakos, G. Á., Hartman, J. D., et al. 2010, ApJ, 720, 1118
Buchhave, L. A., Latham, D. W., Johansen, A., et al. 2012, Natur, 486, 375
Charbonneau, D., Brown, T. M., Latham, D. W., & Mayor, M. 2000, ApJL, 529, L45
Collins, K. A., Kielkopf, J. F., Stassun, K. G., & Hessman, F. V. 2017, AJ, 153, 77
Cooke, B. F., Pollacco, D., West, R., McCormac, J., & Wheatley, P. J. 2018, A&A, 619, A175
Csizmadia, S., Pasternacki, T., Dreyer, C., et al. 2013, A&A, 549, A9
Deleuil, M., & Fridlund, M. 2018, in Handbook of Exoplanets, ed. H. J. Deeg & J. A. Belmonte (Berlin: Springer), 79
Demory, B.-O., & Seager, S. 2011, ApJS, 197, 12
Djupvik, A. A., & Andersen, J. 2010, Astrophysics and Space Science Proceedings, Vol. 14, Highlights of Spanish Astrophysics V (Berlin: Springer), 211
Dressing, C. D., & Charbonneau, D. 2015, ApJ, 807, 45
Droege, T. F., Richmond, M. W., Sallman, M. P., & Creager, R. P. 2006, PASP, 118, 1666
Eastman, J., 2017 EXOFASTv2: Generalized Publication-quality Exoplanet Modeling Code, Astrophysics Source Code Library, ascl:1710.003
Eastman, J., Gaudi, B. S., & Agol, E. 2013, PASP, 125, 83
Espinoza, N., Rabus, M., Brahm, R., et al. 2017, MNRAS, 471, 4374
Fan, Z., Wang, H., Jiang, X., et al. 2016, PASP, 128, 115005
Foreman-Mackey, D., Hogg, D. W., Lang, D., & Goodman, J. 2013, PASP, 125, 306
Fressin, F., Torres, G., Charbonneau, D., et al. 2013, ApJ, 766, 81
Fürész, G. 2008, Phd thesis, University of Szeged
Gaia Collaboration 2018, yCat, none, I/345
Gaia Collaboration 2022, yCat, none, I/357
Gao, D.-Y., Ji, H.-X., Cao, C., et al. 2016, PASP, 128, 125002
Grieves, N., Bouchy, F., Lendl, M., et al. 2021, A&A, 652, A127
Hopp, U., Bender, R., Grupp, F., et al. 2014, Proc. SPIE, 9145, 91452D
Horne, K. 2003, in ASP Conf. Ser. 294, Scientific Frontiers in Research on Extrasolar Planets, ed. D. Deming & S. Seager (San Francisco, CA: ASP), 361
Howell, S. B. 2006, Handbook of CCD Astronomy, Vol. 5 (Cambridge: Cambridge Univ. Press)
Howell, S. B., Everett, M. E., Sherry, W., Horch, E., & Ciardi, D. R. 2011, AJ, 142, 19
Howell, S. B., Matson, R. A., Ciardi, D. R., et al. 2021, AJ, 161, 164
Howell, S. B., Sobeck, C., Haas, M., et al. 2014, PASP, 126, 398
Hu, S.-M., Han, S.-H., Guo, D.-F., & Du, J.-J. 2014, RAA, 14, 719
Huang, F., Li, J.-Z., Wang, X.-F., et al. 2012, RAA, 12, 1585
Hunter, J. D. 2007, CSE, 9, 90
Jenkins, J. M., Twicken, J. D., McCauliff, S., et al. 2016, Proc. SPIE, 9913, 99133E
Kaltenegger, L., & Traub, W. A. 2009, ApJ, 698, 519
Kanodia, S., & Wright, J. T., 2018 Barycorrpy: Barycentric Velocity Calculation and Leap Second Management, Astrophysics Source Code Library, ascl:1808.001
Kharchenko, N. V. 2001, KFNT, 17, 409
Kipping, D. M. 2010, MNRAS, 408, 1758
Kurucz, R. L. 1992, in The Stellar Populations of Galaxies, ed. B. Barbuy & A. Renzini, Vol. 149 (Dordrecht: Kluwer Academic Publishers), 225
Lester, K., Howell, S., Ciardi, D., et al. 2021a, AAS Meeting Abstracts, 53, 344.01
Lester, K. V., Matson, R. A., Howell, S. B., et al. 2021b, AJ, 162, 75
Mazeh, T., Holczer, T., & Faigler, S. 2016, A&A, 589, A75
Miller, N., & Fortney, J. J. 2011, ApJL, 736, L29
Morris, R. L., Twicken, J. D., Smith, J. C., et al. 2020, in Kepler Data Processing Handbook: Photometric Analysis, Kepler Science Document KSCI-19081-003, ed. J. M. Jenkins (California: Kepler Project Office), 6
Naef, D., Latham, D. W., Mayor, M., et al. 2001, A&A, 375, L27
Narita, N., Fukui, A., Kusakabe, N., et al. 2019, JATIS, 5, 015001
Owen, J. E., & Wu, Y. 2013, ApJ, 775, 105
Paegert, M., Stassun, K. G., Collins, K. A., et al. 2021, arXiv:2108.04778
Parviainen, H. 2015, MNRAS, 450, 3233
Pont, F., Hébrard, G., Irwin, J. M., et al. 2009, A&A, 502, 695
Rasio, F. A., Nicholson, P. D., Shapiro, S. L., & Teukolsky, S. A. 1992, Natur, 355, 325
Steuer, J., Kellermann, H., Grupp, F., et al. 2021, Proc. SPIE, 11823, 118231U
Szentgyorgyi, A. H., Geary, J. G., Latham, D. W., et al. 2005, AAS Meeting Abstracts, 207, 110.10
Telting, J. H., Avila, G., Buchhave, L., et al. 2014, AN, 335, 41
Tingley, B. 2004, A&A, 425, 1125
Tody, D. 1986, Proc. SPIE, 627, 733
Trifonov, T., 2019 The Exo-Striker: Transit and Radial Velocity Interactive Fitting Tool for Orbital Analysis and N-body Simulations, Astrophysics Source Code Library, ascl:1906.004
Tuomi, M., Jones, H. R. A., Barnes, J. R., Anglada-Escudé, G., & Jenkins, J. S. 2014, MNRAS, 441, 1545
Tuomi, M., Jones, H. R. A., Butler, R. P., et al. 2019, arXiv:1906.04644
Twicken, J. D., Clarke, B. D., Bryson, S. T., et al. 2010, Proc. SPIE, 7740, 774023
van der Walt, S., Colbert, S. C., & Varoquaux, G. 2011, CSE, 13, 22
Zhang, J.-C., Ge, L., Lu, X.-M., et al. 2015, PASP, 127, 1292
Zhao, F., Zhao, G., Liu, Y., et al. 2019, MNRAS, 482, 1406
Zheng, J. J. L. Q. 2023, AR&T, 20, 83